

# UC Santa Barbara

## UC Santa Barbara Previously Published Works

### Title

Effects of channel morphology and sensor spatial resolution on image-derived depth estimates

### Permalink

<https://escholarship.org/uc/item/69h2296c>

### Journal

Remote Sensing of Environment, 95(2)

### ISSN

0034-4257

### Authors

Legleiter, Carl J.  
Roberts, D A

### Publication Date

2005-03-01

Peer reviewed



## Effects of channel morphology and sensor spatial resolution on image-derived depth estimates

Carl J. Legleiter<sup>a,b,\*</sup>, Dar A. Roberts<sup>a</sup>

<sup>a</sup>Geography Department, University of California Santa Barbara, Ellison Hall 3611, Santa Barbara, CA 93106, United States

<sup>b</sup>Yellowstone Ecological Research Center, Bozeman, MT 59715, United States

Received 18 August 2004; received in revised form 20 December 2004; accepted 24 December 2004

### Abstract

The utility of remote sensing in the study of fluvial systems depends upon the extent to which image data can be used to derive quantitative information of sufficient accuracy and precision for specific applications. In this study, we evaluate the effects of channel morphology on depth retrieval by coupling a radiative transfer model to various morphologic scenarios. Upwelling radiance  $L_u$  spectra generated for a range of depths (2–150 cm) and benthic cover types (limestone, periphyton, and gravel) were linearly mixed to simulate sub-pixel bed topography and substrate heterogeneity. For sloping bottoms, solar-streambed geometry modified  $L_u$  relative to a level bottom, especially for beds sloping steeply away from the sun. Aggregate pixel scale  $L_u$  spectra were compared to a database of simulated spectra to determine the radiance-equivalent depth of a uniform bottom (*REDUB*). *REDUB* spectra for hypothetical stepped streambeds indicated underestimation of the actual area-weighted mean depth, but the  $\ln(L_{u,560}/L_{u,690})$  *REDUB* ratio consistently reproduced the pixel-scale mean for beta distributions of depths. Similarly, when both dark periphyton and bright limestone substrates occurred within a pixel, *REDUB* spectra produced large errors while the ratio proved robust. Along channel banks, pixels will inevitably be mixed, and our simulations indicated that although bank fractions estimated by spectral mixture analysis were highly accurate for vegetated cutbanks, gravel bars were sensitive to the selection of both aquatic and terrestrial end members and subject to relatively large fraction errors. These theoretical results were tested using a ratio-based relative depth map and two-end member mixture models derived from a hyperspectral image of the Lamar River in Yellowstone National Park, which also served to illustrate the importance and applicability of our simulations. The primary conclusions of this study are that 1) the ratio-based algorithm is well-suited to complex river channels; 2) channel morphology and sensor spatial resolution must be considered jointly during data collection and analysis; and 3) the accuracy and precision of depth estimates are influenced by channel morphology and thus vary spatially.

© 2005 Published by Elsevier Inc.

**Keywords:** River channel; Remote sensing; Depth; Radiative transfer model; Spectral mixture analysis; In-stream habitat

### 1. Introduction

Remote sensing has emerged as a potentially powerful tool for detailed, quantitative characterization of fluvial systems across broad geographic areas with improved temporal coverage (Mertes, 2002). Since the early 1990's,

numerous studies have demonstrated the utility of remotely sensed data for retrieving suspended sediment concentrations (Mertes et al., 1993), classifying in-stream habitat (Legleiter & Goodchild, In press; Whited et al., 2002; Wright et al., 2000), and estimating water depth (Lyon et al., 1992; Marcus et al., 2003; Winterbottom & Gilvear, 1997). When multi-temporal image data are available, the synoptic perspective offered by aerial platforms has allowed geomorphologists to document channel changes associated with flood events (Bryant & Gilvear, 1999) and estimate volumes of erosion and deposition in large, braided river systems (Lane et al., 2003). Recent increases in the number and

\* Corresponding author. Geography Department, University of California Santa Barbara, Ellison Hall 3611, Santa Barbara, CA 93106, United States.

E-mail addresses: carl@geog.ucsb.edu (C.J. Legleiter), dar@geog.ucsb.edu (D.A. Roberts).

47 diversity of remote sensing systems, including high spatial  
48 resolution commercial satellites, imply that spectrally-  
49 driven, image-based analyses could become an integral  
50 component of river research and management.

51 Ultimately, however, the utility of remote sensing  
52 technology will depend on the degree to which the channel  
53 characteristics of interest can be remotely measured with the  
54 accuracy and precision required for specific applications.  
55 Although most previous stream research has been empirical,  
56 relating image-derived quantities to ground-based measure-  
57 ments (Marcus et al., 2003; Winterbottom & Gilvear, 1997),  
58 a more thorough knowledge of the underlying physical  
59 principles is needed to quantify uncertainties and define  
60 realistic operational guidelines. As a first step toward a  
61 general theoretical framework, Legleiter et al. (2004) used a  
62 radiative transfer model to illustrate the effects of water  
63 depth, substrate reflectance, suspended sediment, and sur-  
64 face turbulence on the upwelling spectral radiance from a  
65 shallow stream channel. We concluded that, although certain  
66 fundamental limitations must be acknowledged, remote  
67 mapping of river channel morphology and in-stream habitat  
68 is both theoretically sound and technically feasible. In  
69 particular, our radiative transfer simulations and ground-  
70 based spectral measurements demonstrated that a simple  
71 ratio-based algorithm could provide an image-derived  
72 quantity linearly related ( $R^2=0.79$ ) to water depth across a  
73 range of stream conditions.

74 Our initial work described radiative transfer processes  
75 and discussed the role of sensor spectral and radiometric  
76 resolution but did not specifically address the spatial effects  
77 that could prove to be a limiting factor in small-to  
78 moderate-sized channels (Legleiter et al., 2002; Wright et  
79 al., 2000). In these highly variable, dynamic systems, biotic  
80 and geomorphic patterns and interactions often occur at a  
81 spatial scale finer than the spatial resolution of the imaging  
82 system, typically equated with the pixel edge dimension  
83 (but see Cracknell, 1998). Such incongruence between the  
84 scales at which data are collected and processes operate  
85 represents a classic problem in remote sensing and geo-  
86 graphic information science that has also drawn attention in  
87 the marine research community (e.g., Andrefouet et al.,  
88 2002). Recent emphasis on shallow coastal environments,  
89 primarily coral reefs (e.g., Andrefouet et al., 2003), has  
90 motivated studies on the effects of bottom morphology and  
91 fine-scale substrate variability (Mobley & Sundman, 2003;  
92 Zaneveld & Boss, 2003).

93 In this paper, we draw upon coastal research to evaluate a  
94 fundamental question: can remotely sensed data be used to  
95 effectively document the subtle channel changes of interest  
96 to the fluvial geomorphologist? For applications such as  
97 post-project appraisal of river restoration projects (Downs &  
98 Kondolf, 2002) and morphologic estimation of sediment  
99 transport rates (Ashmore & Church, 1998; Gaeuman et al.,  
100 2003), accurate characterization of channel bed topography  
101 is critical (Lane, 1998). The use of raster-formatted image  
102 data in these studies entails two basic limitations: 1) even

when depth varies on a sub-pixel scale, only one depth  
estimate can be assigned to each image pixel; and 2) along  
channel banks, radiance is contributed from both terrestrial  
and aquatic features and pixels will inevitably be mixed.  
The former problem is expected to complicate depth  
retrieval to a degree dependent upon the complexity of  
channel bed topography and benthic cover and the  
dimensions of an image pixel, whereas the latter problem  
could influence measurements of channel width and  
preclude near-bank depth estimates. Our goal in this paper  
is to evaluate the effects of channel morphology and sensor  
spatial resolution on image-derived depth estimates. Specif-  
ically, we use tools developed by oceanographic and  
terrestrial remote sensing scientists—radiative transfer  
modeling and spectral mixture analysis, respectively—to  
address a pair of basic questions:

- 1) When depth or substrate reflectance varies within an  
image pixel, what is the composite upwelling spectral  
radiance signal recorded by a remote sensing system?  
What will be the resulting, single depth estimate for that  
pixel?
- 2) What are the spectral characteristics of mixed pixels  
along channel banks? Can these pixels be unmixed to  
refine estimates of channel width?

## 2. Methods

### 2.1. Field data collection and archival image data

The Lamar River basin of northeastern Yellowstone  
National Park, USA, has been the subject of several  
previous remote sensing studies (e.g., Marcus et al., 2003;  
Wright et al., 2000) and ongoing research on channel  
change. The field data for this study were acquired along  
Soda Butte Creek, a major tributary of the Lamar River, in  
July and August, 2003, and consist of point measurements  
of water depth and a spectral library of channel substrates  
and bank cover types (Fig. 1, Table 1). The collection and  
processing of the spectral data are described in Legleiter et  
al. (2004). Water depths in Soda Butte Creek averaged 38  
cm, with a slightly positively skewed distribution and a  
maximum of 142 cm; the Lamar River is slightly deeper on  
average, with a maximum measured depth of 160 cm  
(Marcus et al., 2003). The substrate in these streams  
consisted primarily of gravel derived from glacial outwash,  
andesitic volcanic rocks, and Paleozoic carbonates (Prostka  
et al., 1975); a few reaches of Soda Butte Creek flow over  
limestone bedrock. As flows subside in mid- to late summer,  
periphyton coats portions of the streambed as well, typically  
in shallow, low-velocity areas.

Hyperspectral image data for the Lamar River were  
acquired by the AISA sensor on August 1, 2002. This  
instrument recorded upwelling spectral radiance in 34  
narrow bands (full-width half-maximum of 3.10–3.42 nm)

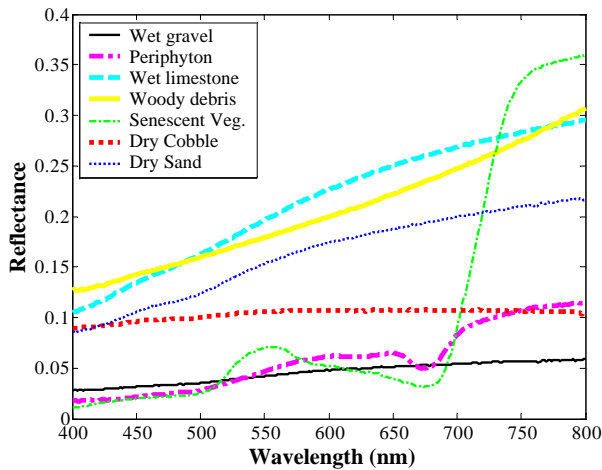


Fig. 1. Reflectance spectra for substrate types and stream bank materials from the spectral library compiled along Soda Butte Creek in Yellowstone National Park (Legleiter et al., 2004).

156 spanning the visible/near-infrared spectral region from 495–  
 157 898 nm. Apparent at-platform reflectance was calculated  
 158 from concurrent measurements of downwelling spectral  
 159 irradiance, obtained using a diffuse collector mounted on  
 160 top of the aircraft and connected to the AISA sensor by a  
 161 fiber optic cable (<http://www.specim.fi/products-aisa.html>).  
 162 The ground sampling distance of 2.5 m produced many  
 163 mixed pixels along the banks of the 30–50 m wide channel  
 164 and dictated that most in-stream pixels would encompass a  
 165 range of depths and/or substrate types. Although ground  
 166 reference data for this time period were not available, we  
 167 intend to use the AISA image as part of a time series for  
 168 monitoring channel change in northern Yellowstone. Here,  
 169 we present a scene from the Lamar River to evaluate the  
 170 results of the radiative transfer simulations that are the  
 171 primary focus of this paper and to illustrate the real-world  
 172 applicability of these modeled scenarios.

173 *2.2. Radiative transfer modeling*

174 In essence, passive optical remote sensing of fluvial  
 175 systems is based upon spatially distributed measurements  
 176 of a fundamental physical quantity, the upwelling spectral  
 177 radiance. For a shallow stream channel, this reflected solar  
 178 energy can be conceptualized as the sum of four  
 179 components:

$$L_T = L_P + L_S + L_C + L_B + L_L, \quad (1)$$

180 where  $L_T$  is the total at-sensor spectral radiance;  $L_P$   
 182 represents path radiance scattered into the sensor’s field  
 183 of view by the Earth’s atmosphere;  $L_S$  denotes radiance  
 184 reflected from the water surface, interacting with neither  
 185 the water column nor the substrate;  $L_C$  refers to radiance  
 186 that entered the water column but was scattered into the  
 187 upper hemisphere before reaching the bottom;  $L_B$  is the  
 188 portion of  $L_T$  that reflected from the streambed, passed  
 189 through the air–water interface, and traveled through the

atmosphere to the sensor; and  $L_L$  is the radiance  
 190 contribution from adjacent areas of land, typically gravel  
 191 bars or riparian vegetation, for mixed pixels along the  
 192 channel banks. Of these components, only the last is  
 193 directly relevant to characterization of channel morphology  
 194 (i.e., water depth) and in-stream habitat (i.e., benthic  
 195 cover). Our analysis thus focused upon the two primary  
 196 controls on  $L_B$ , bottom depth  $z_b$  and the (spectral  
 197 irradiance) reflectance of the substrate  $R_\lambda$ , by using a  
 198 radiative transfer model to simulate  $L_T$  spectra while fixing  
 199 the parameters that determine  $L_P$ ,  $L_S$ ,  $L_C$ , and  $L_L$ .  
 200

201 The radiative transfer equation describes the attenuation  
 202 of electromagnetic radiation within the water column and  
 203 can be solved numerically, subject to certain critical  
 204 assumptions, if initial and boundary conditions are specified  
 205 (Mobley, 1994). The Hydrolight computer model (Mobley  
 206 & Sundman, 2001) implements these solution methods to  
 207 simulate spectral radiance distributions within and above a  
 208 water column and is used extensively in various marine  
 209 environments (e.g., Dierssen et al., 2003; Louchard et al.,  
 210 2003). Individual Hydrolight runs are parameterized by  $z_b$ ,  
 211 and  $R_\lambda$ , as well as water column optical properties, water  
 212 surface state, solar geometry, and atmospheric conditions.  
 213 This one-dimensional model assumes that all changes in the  
 214 underwater light field are functions of depth alone,  
 215 independent of horizontal location; this simplified geometry

Table 1  
 Input parameters for the Hydrolight radiative transfer model

| Parameter type   | Value or range of inputs  | Description  |       |
|--|---------------------------|--|-------|
| Solar geometry   | 20°, 30°, 40°, 50°, 60°   | Solar zenith angle in air  | t1.4  |
| Sea level pressure   | 1016 mbar                 |  | t1.5  |
| Air mass type  | 10                        | Continental  | t1.6  |
| Relative humidity  | 20%                       |  | t1.7  |
| Precipitable water   | 0.5 cm                    |  | t1.8  |
| 24-hr average wind speed                                   | 0 m/s                     |  | t1.9  |
| Horizontal visibility                                      | 100 km                    |  | t1.10 |
| Water depth  | 2–150 cm in steps of 1 cm |  | t1.11 |
| Substrate reflectance (ground-based spectral measurements) | Periphyton                | Samples scraped from cobbles removed from streambed  | t1.12 |
|  | Wet gravel                | Mixture of rock types and particle sizes, measured on gravel bars  | t1.13 |
|  | Wet limestone             | Mississippian Madison Limestone Group (Prostka et al., 1975); Grey-white (Munsell color chart: Hue 0.19Y, Value 5.71, Chroma 2.87) | t1.14 |
| Suspended sediment concentration                           | 2 g/m <sup>3</sup>        | Converted to inherent optical properties using brown earth optical cross-section   | t1.15 |
| Wind speed   | 5 m/s                     | Surrogate for flow turbulence  | t1.16 |



allows for numerical solution of the radiative transfer equation. For more complex, three-dimensional configurations where bottom depth and/or albedo vary spatially (i.e., river channels), computationally expensive probabilistic methods are technically more appropriate. Mobley and Sundman (2003), however, found close agreement between Hydrolight and a backward Monte Carlo model (BMC3D) in the presence of fine-scale substrate variability (errors < 1%) and sloping bottoms (errors < 7% for bottom slopes < 20°), concluding that efficient one-dimensional models can predict radiance distributions above heterogeneous bottoms with sufficient accuracy for all but the most demanding applications. For our first-order analysis, we therefore adopt this plane-parallel approximation and use the Hydrolight radiative transfer model to simulate the effects of sub-pixel variability of depth and bottom albedo.

We developed a database of 2,235 simulated Hydrolight spectra parameterized by the input data in Table 1. The incident spectral irradiance  $E_d$  and sky radiance distribution for our study area in Yellowstone National Park were obtained using the Gregg and Carder (1990) and Harrison and Coombes (1988) models, respectively; cloud cover was assumed negligible. To isolate the effects of depth and bottom albedo, suspended sediment concentration was fixed at 2 g/m<sup>3</sup> and the brown earth optical cross-section included with Hydrolight used to obtain the corresponding absorption ( $a$ ) and scattering ( $b$ ) coefficients (Bukata et al., 1995). The concentration profile was vertically homogeneous and the contributions of chlorophyll and dissolved organic matter to the inherent optical properties of the water column were assumed negligible. In practice, the abundance and wavelength-dependent scattering and absorption properties of various constituents suspended and/or dissolved within the flow will also influence  $L_u$  and thus depth retrieval and substrate characterization. Surface turbulence was incorporated by fixing the wind speed, which Hydrolight uses to generate an irregular water surface described by the Cox and Munk (1954) wave slope statistics (Mobley, 1994), at 5 m/s. Substrate  $R_\lambda$  spectra for three bottom types were used, including bright white-gray limestone, periphyton scraped from streambed cobbles, and gravel of mixed grain size and lithology (Fig. 1, Table 1). For each substrate type, simulated spectra were generated for bottom depths ranging from 2 to 150 cm in 1 cm increments. Shallower and/or more closely spaced depths could not be modeled because Hydrolight computes diffuse attenuation coefficients (e.g.,  $K_d$ , defined as the depth derivative of the downwelling plane irradiance  $E_d$ ; Mobley, 1994) using a finite difference approximation that dictates a minimum spacing between successive output depths. All depths shallower than 2 cm in our simulations were therefore assigned the corresponding  $L_u$  spectra for a depth of 2 cm. To evaluate the effect of solar geometry, a separate set of Hydrolight runs for all depth/substrate combinations was performed for in-air solar zenith angles  $\theta_s$  from 20° to 60°, in 10° increments. The modeled

spectra spanned the range 400–800 nm as a series of 100 monochromatic runs spaced 4 nm apart.

### 2.3. Simulated spectral mixtures

We examined the effects of sub-pixel variation of depth and bottom albedo and mixed stream bank pixels by simulating spectral mixtures, with an assumption of linear mixing. Under this framework, the composite spectral radiance  $L_\lambda$  from a pixel containing multiple cover types (or bottom depths) is the sum of the  $L_\lambda$  for each cover type, weighted by their areal abundance—that is, the spectral proportions match the spatial proportions (Adams et al., 1993). The use of additive mixtures neglects the contribution of multiply scattered photons to the total radiance, and our simulated mixtures therefore do not account for in-water adjacency effects. In shallow stream channels, however, these effects are likely to be minimal because the scattering phase function is strongly forward-peaked and depths are typically only one or two photon mean free paths  $1/c$ , where  $c = a + b$  is the beam attenuation coefficient (Mobley & Sundman, 2003). Mobley and Sundman (2003, p.333) argued that under these circumstances, the vast majority of photons travel directly from the bottom to the water surface and the path radiance contribution is negligible, implying that scattering by the water column itself can be ignored. The validity of this assumption will be strained in deeper water and/or for higher suspended sediment concentrations, but provides a reasonable approximation for the shallow, clear water conditions in our study area.

Using the database of simulated Hydrolight spectra, we assembled fine-scale radiance fields by assigning the appropriate upwelling radiance  $L_u$  (in air, just above the water surface) spectrum to each cell of various morphologic scenarios. Mixed pixels were then simulated by computing the average of the  $L_u$  values for all 1 cm<sup>2</sup> cells encompassed by a pixel of the specified dimensions. We assumed square pixels and equally weighted the radiance contributions of all cells within the pixel; a more sophisticated radiance aggregation scheme could be used to model the point spread function of a particular sensor. For the stream bank scenarios, mixtures were modeled by combining the field-measured  $R_\lambda$  spectra for the bank material types with  $R_\lambda$  spectra for the submerged portion of the pixel, obtained from the Hydrolight-modeled  $L_u$  by converting to irradiance (assuming isotropy and multiplying by  $\pi$ ) and dividing by  $E_d$ .

### 2.4. Morphologic scenarios

Simulated spectra from the Hydrolight database were coupled to various bed configurations to model the effects of solar-streambed geometry, fine-scale morphology, and substrate heterogeneity on the pixel-scale upwelling spectral radiance that would be measured by a remote sensing system. Each scenario consisted of regular grids of depth

272  
273

274

275

276

277

278

279

280

281

282

283

284

285

286

287

288

289

290

291

292

293

294

295

296

297

298

299

300

301

302

303

304

305

306

307

308

309

310

311

312

313

314

315

316

317

318

319

320

321

322

323

324

324 and substrate type with a cell size of 1 cm<sup>2</sup>, and spectral  
 325 properties were assigned from a look-up table. These  
 326 scenarios are described in the following paragraphs and  
 327 illustrated in Fig. 2.

328 To evaluate the effect of solar geometry and streambed  
 329 slope and aspect, we considered a planar streambed rotated  
 330 about both the vertical and horizontal axes. The bed sloped  
 331 down at a specified angle  $\theta_b$  and aspect  $\phi$  was defined as  
 332 the angular difference between the slope direction and solar  
 333 azimuth (Fig. 2a). Mobley and Sundman (2003) reasoned  
 334 that the primary effect of a sloping bottom was to change the  
 335 solar incidence angle and that the slope could be accounted  
 336 for by using Lambert's cosine law to correct the radiance  
 337 computed for a level bottom (i.e., with Hydrolight). We used

Eqs. (9) and (10) of Mobley and Sundman (2003) to 338  
 compute the radiance from a sloping streambed as 339

$$L_u^{\text{slope}} = L_u^{\text{level}} \frac{\cos\theta_i^{\text{slope}}}{\cos\theta_i^{\text{level}}}, \quad (2)$$

where  $\theta_i$  denotes the solar incidence angle onto the 340  
 streambed and the superscripts refer to sloping and level 342  
 bed configurations. For a sloping bed,  $\theta_i$  is given by 343

$$\cos\theta_i^{\text{slope}} = \sin\theta_b \sin\theta_{sw} \cos\phi + \cos\theta_b \cos\theta_{sw}, \quad (3)$$

where  $\theta_{sw}$  is the solar zenith angle after refraction at the air– 344  
 water interface. 346

The effects of sub-pixel depth variability were modeled 347  
 by aggregating fine-scale radiance fields corresponding to a 348  
 stepped streambed. A fraction  $f_{\text{deep}}$  of the simulated pixel 349  
 was assigned a relatively large depth  $z_{\text{deep}}$  while the 350  
 remaining  $1-f_{\text{deep}}$  was assigned a shallower depth  $z_{\text{shallow}}$  351  
 (Fig. 2b). By varying these three parameters, we modeled 352  
 composite, pixel-scale  $L_u$  spectra for pixels ranging from 353  
 predominantly deep to mostly shallow, with various step 354  
 heights (i.e., intra-pixel depth differences); both sides of the 355  
 step had the same substrate  $R_i$  and  $\theta_s$  was fixed at 30°. To 356  
 determine the effect of such sub-pixel morphologic features 357  
 on depth retrieval, we compared the composite radiance 358  
 from the stepped streambed to the  $L_u$  spectra tabulated in the 359  
 Hydrolight database by defining the radiance-equivalent 360  
 depth of a uniform bottom (*REDUB*) for each wavelength as 361  
 the depth at which  $L_u$  from a flat bed is closest in absolute 362  
 value to the composite radiance from a more topographically 363  
 complex streambed. 364

More complex bed configurations were simulated as 365  
 random variables drawn from a beta distribution defined by 366  
 parameters  $\alpha$  and  $\beta$  and bounded by a specified minimum 367  
 $z_{\text{min}}$  and maximum  $z_{\text{max}}$  depth 368

$$f(z_b; \alpha, \beta, z_{\text{min}}, z_{\text{max}}) = \frac{1}{z_{\text{max}} - z_{\text{min}}} \cdot \frac{\Gamma(\alpha + \beta)}{\Gamma(\alpha)\Gamma(\beta)} \times \left( \frac{z_b - z_{\text{min}}}{z_{\text{max}} - z_{\text{min}}} \right)^{\alpha-1} \times \left( \frac{z_{\text{max}} - z_b}{z_{\text{max}} - z_{\text{min}}} \right)^{\beta-1}, \quad (4)$$

where  $f(\cdot)$  is the probability density function (pdf) of depths 369  
 for  $z_{\text{min}} \leq z_b \leq z_{\text{max}}$  (the beta distribution has zero density 371  
 outside this interval), and  $\Gamma(\cdot)$  is the gamma function 372  
 (Devore, 2000). A single substrate reflectance was used for 373  
 all 1 cm<sup>2</sup> cells and  $\theta_s$  was fixed at 30°. The flexibility of the 374  
 beta pdf allowed us to generate depth histograms skewed 375  
 toward deep or shallow water, uniformly distributed across 376  
 the specified range of depths, or centered about a single 377  
 mean depth. To examine the effects of differing degrees of 378  
 sub-pixel scale topographic complexity on depth retrieval, 379  
 we used the log-transformed band ratio algorithm shown to 380  
 provide an image-derived quantity linearly related to water 381  
 depth (Legleiter et al., 2004), computing  $\ln(L_{u,560}/L_{u,690})$  382

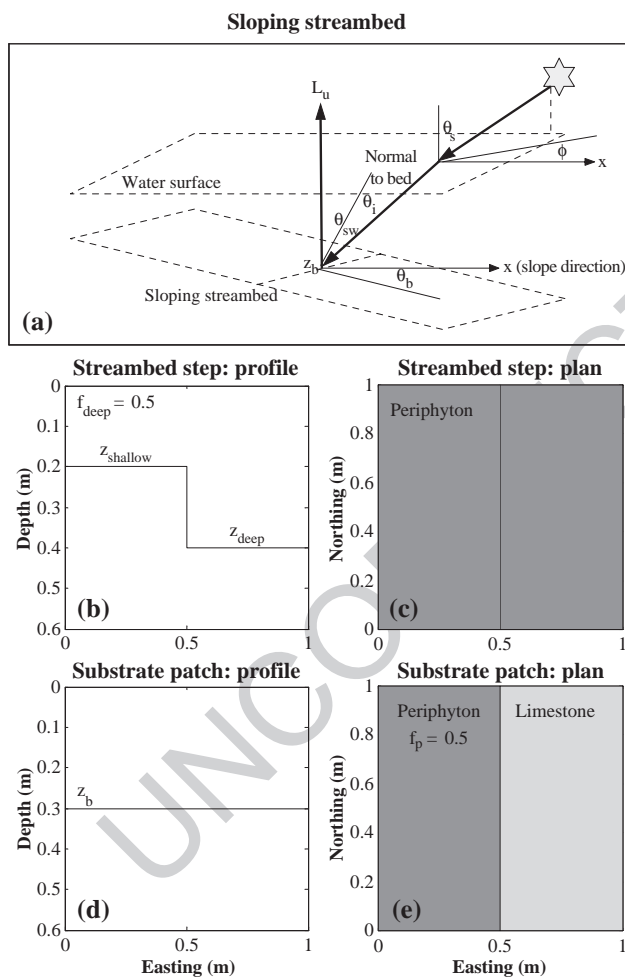


Fig. 2. Basic morphologic scenarios evaluated in this study. (a) A planar, sloping bed for modeling the effects of solar-streambed geometry. The bed slopes down in the x direction at an angle of  $\theta_b$  with the horizontal, the depth at which the upwelling spectral radiance  $L_u$  is modeled as  $z_b$ , the solar zenith angle is  $\theta_s$  in air and  $\theta_{sw}$  in water, the solar azimuth (angular difference between the slope direction and the position of the sun) is  $\phi$ , and the incidence angle of the solar beam onto the streambed is  $\theta_i$ , measured relative to the streambed normal. Profile (b) and plan (c) of a stepped streambed with a uniform substrate. Profile (d) and plan (e) of a heterogeneous substrate with a constant depth  $z_b$ . Scenarios evaluated for hypothetical 1 m<sup>2</sup> pixels. Figure after Mobley and Sundman (2003).

383 for both aggregate, pixel-scale radiances for the simulated  
 384 streambeds and for individual  $L_u$  spectra in the Hydrolight  
 385 database. Analogous to the *REDUB* above, we define the  
 386 *REDUB* ratio as the depth at which the log-transformed  
 387 band ratio value computed for a level bottom is closest in  
 388 absolute value to the ratio computed for the mixed, variable  
 389 depth pixel.

390 Similar to the bed step scenario, we modeled the effects  
 391 of sub-pixel substrate heterogeneity by assigning a specified  
 392 fraction of a pixel to one substrate and the remainder to a  
 393 second benthic cover type (Fig. 2c). For these simulations,  
 394 bottom depth was held constant and  $\theta_s$  was fixed at  $30^\circ$ .  
 395 Because  $L_u$  is a function not only of depth but also bottom  
 396 albedo (Legleiter et al., 2004), fine-scale substrate hetero-  
 397 geneity might interfere with depth retrieval. To examine this  
 398 possibility, we computed both wavelength-specific *REDUB*  
 399 values and  $\ln(L_{u,560}/L_{u,690})$  *REDUB* ratio values for  
 400 simulated constant depth/mixed substrate pixels.

#### 401 2.5. Stream bank spectral mixture analysis

402 Along the margins of the channel, radiance is contributed  
 403 from both the submerged streambed and adjacent exposed  
 404 areas with various cover types. In this study, we considered  
 405 two common stream bank configurations which often occur  
 406 in tandem on the inner and outer banks of a meander bend,  
 407 respectively: a gently sloping gravel bar and a steep,  
 408 vegetated cutbank (Fig. 3). We modeled mixed pixels along  
 409 the gravel bar by specifying the fraction of the pixel  $f_b$   
 410 occupied by exposed gravel and the bed slope  $\theta_b$  off the bar  
 411 into the channel, retrieving the appropriate Hydrolight  
 412 spectrum for each depth (depths shallower than 2 cm were

413 assigned the spectrum for 2 cm depth; see Section 2.2) along  
 414 the slope (1 cm<sup>2</sup> cell size), applying the slope correction  
 415 (Eq. (2);  $\theta_s$  fixed at  $30^\circ$  and  $\varphi$  at  $45^\circ$ ), converting the  $L_u$   
 416 spectra to reflectance (Section 2.3), and adding the area-  
 417 weighted reflectances of the submerged and exposed  
 418 portions of the pixel. For the vegetated cutbank, pixel-scale  
 419 mixtures were generated by specifying  $f_b$  and the bottom  
 420 depth  $z_b$ . The transition from bank top to channel bed was  
 421 assumed to occur over a fixed distance of 10 cm, and the  
 422 radiance from this zone was incorporated by computing the  
 423 depths along the slope and applying the slope correction as  
 424 for the gravel bar. The pixel-scale reflectance was obtained  
 425 by summing the area-weighted contributions from the  
 426 vegetated bank, the bank-to-bed submerged slope, and the  
 427 flat streambed.

428 To determine the extent to which stream bank pixels  
 429 can be unmixed on the basis of their spectral character-  
 430 istics, we used spectral mixture analysis (SMA, Adams et  
 431 al., 1993), a popular technique with numerous terrestrial  
 432 applications that has recently been extended to shallow  
 433 marine environments (Hedley & Mumby, 2003; Hedley et  
 434 al., 2004), to estimate  $f_b$  for different bank scenarios. The  
 435 essence of SMA is to model the reflectance (or radiance)  
 436 spectrum of a mixed pixel as a weighted linear combina-  
 437 tion of the spectra of two or more pure cover types, called  
 438 end members:

$$R'_\lambda = \sum_{k=1}^N f_k R_{k\lambda} + \epsilon_\lambda. \quad (5)$$

439 Here,  $R'_\lambda$  is the modeled mixture,  $f_k$  represents the  
 440 fractions of each of  $k$  end members,  $R_{k\lambda}$  is the reflectance  
 441



Fig. 3. Field examples of the stream bank morphologic scenarios evaluated in this study, from the Hollywood Meadow reach of Soda Butte Creek in Yellowstone National Park. Gradually sloping gravel bar in foreground and abrupt, vegetated cutbank on opposite side of channel. Photo courtesy of Dr. Andrew Marcus.



442 spectrum of the  $k$ th end member, and  $\epsilon_\lambda$  is a wavelength-  
 443 specific error term; a unit sum constraint is typically  
 444 imposed on the  $f_k$  as well (Roberts et al., 1998). For our  
 445 analysis of stream bank mixtures, we use Gaussian  
 446 elimination to determine the least-squares optimal two-  
 447 end member model for each bank scenario. One end  
 448 member is the bank material reflectance spectrum and a  
 449 single Hydrolight-modeled spectrum serves as the aquatic  
 450 end member. For the gravel bar scenario, we evaluated the  
 451 sensitivity of the mixture model to aquatic end member  
 452 selection by computing bank fractions using three differ-  
 453 ent water spectra: 1) the Hydrolight spectrum for the  
 454 mean depth along the submerged portion of the bank  
 455 slope, typically 5–10 cm depending on  $f_b$  and  $\theta_b$ ; 2) a  
 456 fixed water spectrum of moderate depth, as might be  
 457 obtained by selecting an image end member from the  
 458 channel talweg; and 3) the spectrum for the greatest depth  
 459 in the Hydrolight database, 1.5 m. For the vegetated  
 460 cutbank, the water end member was taken as the  
 461 Hydrolight spectrum corresponding to the depth of the  
 462 channel bed  $z_b$ . To assess the feasibility of unmixing  
 463 stream bank spectra, we compared the modeled bank  
 464 fractions to the input  $f_b$  used to parameterize each  
 465 simulated bank scenario.

3. Results

466

3.1. Effects of sun-streambed geometry on upwelling spectral radiance

467  
468

In topographically complex, meandering stream channels, the solar irradiance incident upon the channel bed will vary spatially as a function of solar geometry and local streambed slope and aspect. Fig. 4 illustrates the effect of solar-streambed geometry, expressed as the percent difference in  $L_{u,690}$  relative to a flat bed, for a range of in-air solar zenith angles  $\theta_s$ , slope aspects  $\phi$  (defined as the angular difference between the solar azimuth and slope direction), and bed slopes  $\theta_b$ . For low  $\theta_s$  and low to moderate  $\theta_b$ , topographic effects are minimal for small  $\phi$  (i.e., sun shining directly onto the slope) but become substantial for larger  $\phi$ , with the greatest modification of the solar beam's angle of incidence onto the streambed occurring at  $\phi=180^\circ$  when the bed slopes down away from the sun (Mobley & Sundman, 2003). As  $\theta_s$  increases to  $40^\circ$  or  $50^\circ$ ,  $L_u$  can be increased by nearly 20% relative to a flat bottom when a moderately steep bed slope faces the sun or reduced by up to 100% when the aspect is less favorable. For a fixed solar geometry (i.e., time of data collection), topographic effects

469  
470  
471  
472  
473  
474  
475  
476  
477  
478  
479  
480  
481  
482  
483  
484  
485  
486  
487

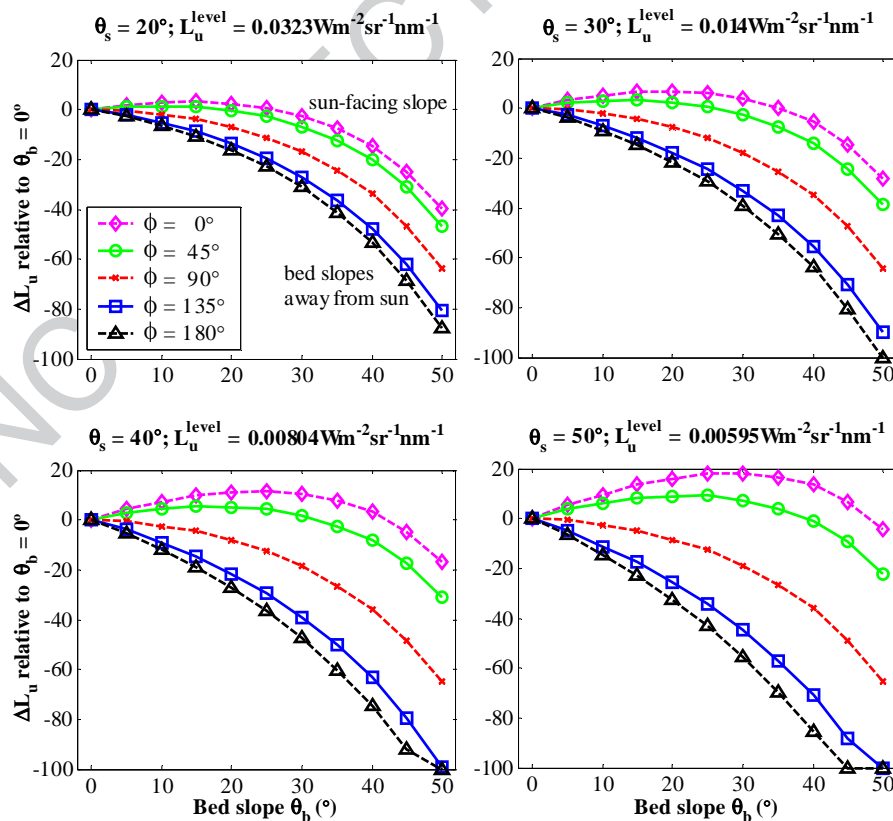


Fig. 4. Effect of solar geometry and streambed slope  $\theta_b$  and aspect  $\phi$  on the upwelling spectral radiance  $L_u$  (at 690 nm) from a shallow stream channel. Each panel represents a different solar zenith angle  $\theta_s$  (in air) and lines represent different aspects  $\phi$ , defined as the angular difference between the solar azimuth and the slope direction. The streambed faces the sun for small  $\phi$  and slopes down away from the sun for large  $\phi$ . Changes in radiance  $\Delta L_u$  are expressed as percentages of the equivalent level bottom  $L_u$ . Depth is 0.3 m and substrate is periphyton.



488 are clearly more pronounced for steeper bed slopes, such as  
 489 those along channel banks. Although bed slopes of  $50^\circ$   
 490 might not be common in alluvial rivers, especially those  
 491 with non-cohesive banks, even for a more typical pool exit  
 492 slope of  $10^\circ$  (e.g., Thompson & Hoffman, 2001) and a fixed  
 493  $\theta_s$ , differences in  $\varphi$  alone could still create a 10–15% range  
 494 in  $L_u$ .

### 495 3.2. Effects of sub-pixel variability in depth

496 For smaller or more complex channels and/or coarser  
 497 sensor spatial resolutions, many, if not most, image pixels  
 498 will encompass relatively fine-scale morphologic features  
 499 and thus a range of depths. For the hypothetical stepped  
 500 streambed in Fig. 2b, the REDUB exhibited spectrally-  
 501 dependent residuals which varied with  $f_{\text{deep}}$  and step height  
 502  $z_{\text{deep}} - z_{\text{shallow}}$  (Fig. 5). For a moderate step height of 20 cm,  
 503 the REDUB matched the area-weighted mean depth (thin,  
 504 dashed lines in Fig. 5) at shorter, blue wavelengths but in the  
 505 red portion of the spectrum positive REDUB residuals,  
 506 defined as the difference between the area-weighted mean  
 507 depth and the REDUB, indicated that depth was under-  
 508 estimated. The magnitudes of these residuals were least (1  
 509 cm) when  $f_{\text{deep}}$  was either large (0.9) or small (0.1) and  
 510 greatest when the pixel contained equal amounts of deep  
 511 and shallow water, up to 3 cm in the near-infrared for  
 512  $0.4 \leq f_{\text{deep}} \leq 0.6$ . The gaps in the REDUB spectra plotted in  
 513 Fig. 5 correspond to a crossover region of equal  $L_u$  for all  
 514 depths, with scattering by suspended sediment dominant at

515 shorter wavelengths and absorption by pure water prevalent  
 516 in the red and near-infrared (Legleiter et al., 2004). As the  
 517 step height increased to 40 or 60 cm, the REDUB residuals  
 518 became increasingly positive, indicating larger underesti-  
 519 mates of the area-weighted mean depth. For the 60 cm step,  
 520 the REDUB bias reached 22 cm in the NIR for  $f_{\text{deep}}=0.7$  and  
 521 was 5 cm even in the visible at 675 nm. For smaller  $f_{\text{deep}}$   
 522 (i.e., shallower area-weighted mean depths), the REDUB  
 523 residuals were smaller but can still be on the order of 8 cm  
 524 for high steps. This effect was also modulated by the  
 525 substrate, and the high NIR reflectance of periphyton also  
 526 could have contributed to the large REDUB residuals in Fig.  
 527 5; the magnitude of these residuals might be reduced for  
 528 other substrates with lower NIR reflectance. In general, for  
 529 pixels with both a range of depths and a non-homogeneous  
 530 substrate, the pixel-scale  $L_u$  will depend on the spatial  
 531 distribution of benthic cover types relative to the bed  
 532 topography, as well as the scattering properties of the water  
 533 column. In any case, our simulations indicated that the  
 534 juxtaposition of deep and shallow water within a single  
 535 pixel caused spectrally-based depth retrieval to under-  
 536 estimate the true mean depth because the shallow water  
 537 made an areally disproportionate contribution to the  
 538 aggregate, pixel-scale radiance, effectively drowning out  
 539 the radiance contributed from the deeper water portion of  
 540 the pixel.

541 We also performed a second, somewhat more realistic set  
 542 of simulations based upon beta distributions of depth within  
 543 an image pixel. By varying the  $\alpha$  and  $\beta$  parameters of the

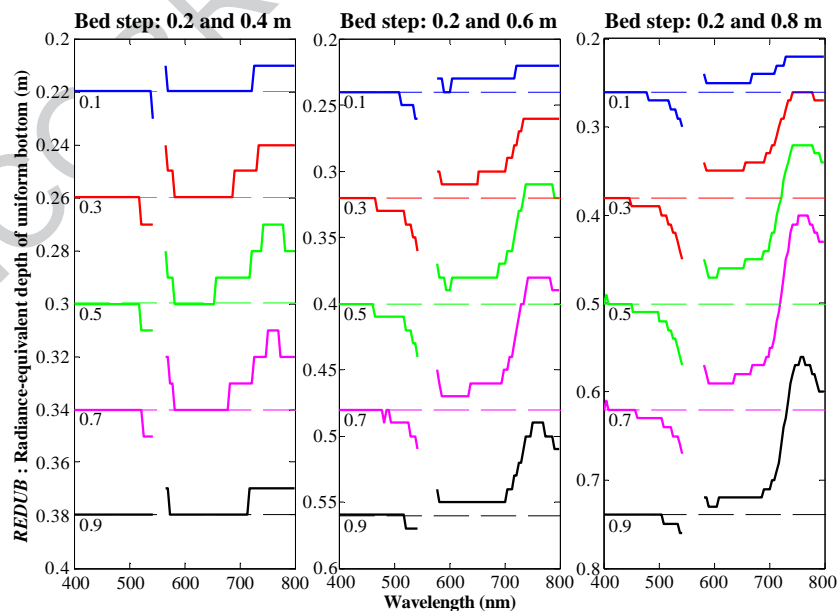


Fig. 5. REDUB spectra for simulated stepped streambeds of various step heights ( $z_{\text{deep}} - z_{\text{shallow}}$ ) and fractions of deep water  $f_{\text{deep}}$  (labeled for each line). The radiance-equivalent depth of a uniform bottom (REDUB) is defined at each wavelength as the depth of a uniform bottom at which the modeled Hydrolight  $L_u$  spectrum is closest in absolute value to the  $L_u$  for the mixed, variable depth pixel. The thin dashed lines in each panel represent the area-weighted mean depth for the specified  $f_{\text{deep}}$  and the REDUB residual is defined as the difference between this true depth and the REDUB at each wavelength. The gap in each REDUB spectrum represents a region of equal radiance for all depths (see text for explanation). Substrate is periphyton and solar zenith angle  $\theta_s$  is  $30^\circ$  (in air). (For interpretation of the references to colour in this figure legend, the reader is referred to the web version of this article.)

544 beta pdf (Eq. (4)), we created depth distributions represen-  
 545 tative of sloping bottoms (uniform pdf; Fig. 6a), relatively  
 546 flat bottoms (strongly peaked, symmetric distribution; Fig.  
 547 6d), and streambed configurations featuring either predom-  
 548 inantly shallow (Fig. 6e) or predominantly deep (Fig. 6f)  
 549 water. The performance of a ratio-based depth retrieval  
 550 algorithm in the presence of such sub-pixel depth variability  
 551 was evaluated in terms of the *REDUB* ratio, the depth of a  
 552 uniform bottom for which the  $\ln(L_{u,560}/L_{u,690})$  ratio is  
 553 equivalent to that computed for the simulated pixel. The  
 554 *REDUB* ratio consistently reproduced the area-weighted  
 555 mean depth of the pixel, even for negatively skewed depth  
 556 distributions (Fig. 6f, h), unlike the spectrally-dependent  
 557 residuals observed when the *REDUB* was retrieved from the  
 558 Hydrolight database on a band-by-band basis.

### 559 3.3. Effects of sub-pixel variability in bottom albedo

560 Because  $L_u$  is sensitive to both depth and bottom  
 561 albedo, sub-pixel substrate heterogeneity could influence

562 spectrally-based depth estimates even when depth is 562  
 563 uniform at the pixel scale. Reflectance spectra for pure 563  
 564 limestone and periphyton substrates are plotted in Fig. 7a 564  
 565 and the panels below contain *REDUB* spectra (lines) and 565  
 566 *REDUB* ratio depth estimates (points) for mixtures of these 566  
 567 two substrate end members at depths of 30 and 60 cm 567  
 568 (indicated by the dashed line in each panel). Fig. 7b and d 568  
 569 illustrate the results of simulating  $L_u$  for a mixed substrate 569  
 570 comprised of both periphyton (covering a fraction  $f_p$  of the 570  
 571 substrate) and limestone (covering the remaining  $1-f_p$ ), 571  
 572 but then restricting the search of the Hydrolight database 572  
 573 to consider only the pure periphyton end member when 573  
 574 retrieving the *REDUB* for the mixed pixel. Similarly,  $L_u$  574  
 575 spectra for these periphyton/limestone mixtures were 575  
 576 compared to the pure limestone end members in the 576  
 577 Hydrolight database to obtain the *REDUB* spectra and 577  
 578 *REDUB* ratio values shown in Fig. 7c and e; *REDUB* 578  
 579 retrievals were limited to depths less than 1 m in all cases. 579  
 580 In essence, this analysis quantifies the depth retrieval error 580  
 581 that would be incurred if substrate heterogeneity were 581

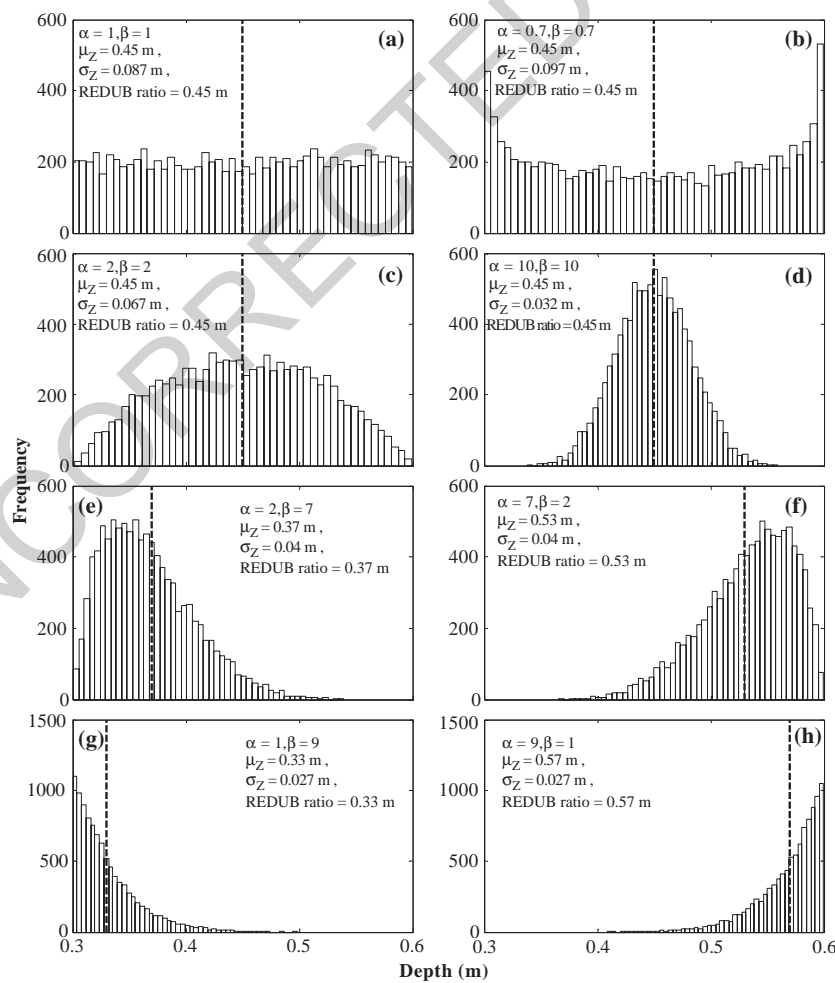


Fig. 6. Effects of sub-pixel bottom topography, simulated using beta distributions, on ratio-based depth retrieval. The dashed lines in each panel correspond to the *REDUB* ratio, defined as the depth of a uniform bottom for which the  $\ln(L_{u,560}/L_{u,690})$  ratio calculated for a Hydrolight spectrum is equivalent to that computed for the simulated, variable-depth pixel. Each panel also lists the parameters ( $\alpha$  and  $\beta$ ) used to generate the depth distribution, the area-weighted mean depth  $\mu_z$ , and the standard deviation of depth  $\sigma_z$ . Substrate is periphyton and  $\theta_s=30^\circ$  (in air).

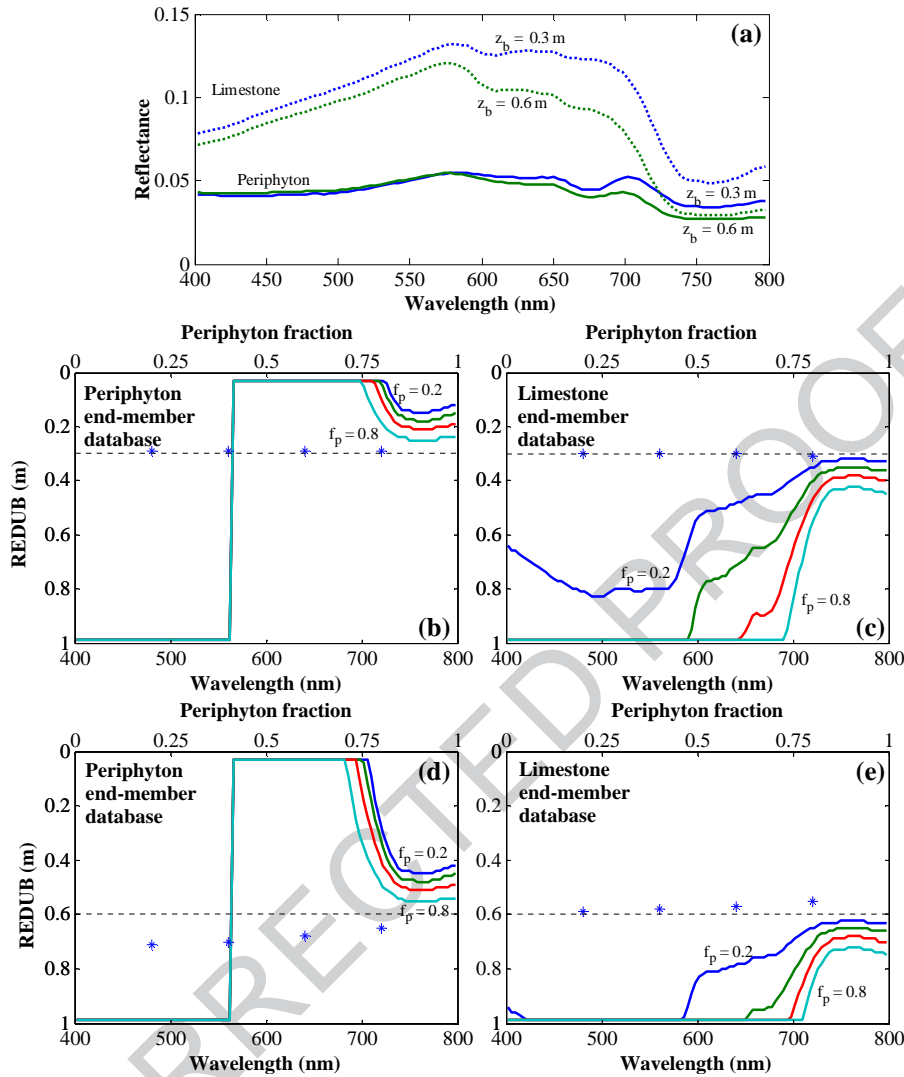


Fig. 7. Effects of fine-scale substrate heterogeneity on spectrally-based depth estimates. (a) Hydrolight-modeled reflectance spectra for limestone and periphyton substrates at depths of 30 and 60 cm. (b–d) *REDUB* spectra (lines, referring to bottom axis, with the periphyton fraction  $f_p$  for each line labeled on the plot) and *REDUB* ratio values (points, referring to top x-axis) for various periphyton fractions, using both pure periphyton (b and d) and pure limestone spectra (c and e) from the Hydrolight database as references for comparison with the simulated limestone/periphyton mixtures. Bottom is level at the depth indicated by the dashed line in each panel and  $\theta_s$  is fixed at  $30^\circ$  (in air). (For interpretation of the references to colour in this figure legend, the reader is referred to the web version of this article.)

582 neglected and a single benthic end member was used  
583 throughout an image.

584 When comparing the simulated constant depth/mixed  
585 substrate  $L_u$  spectra to the pure periphyton database, the  
586 *REDUB* “saturated” and was assigned the greatest depth in  
587 the database at wavelengths up to 560 nm, irrespective of  
588 the actual bottom depth or  $f_p$  of the simulated mixture. At  
589 this end of the spectrum, an increase in  $z_b$  corresponded to  
590 an increase in  $L_u$  due to scattering by suspended sediment,  
591 and the increased pixel-scale  $L_u$  due to the presence of  
592 bright limestone had the same effect as an increase in  
593 volume reflectance and effectively caused the pixel to  
594 appear deeper than if the substrate were composed of pure  
595 periphyton. Conversely, in the red portion of the spectrum  
596  $L_u$  and  $z_b$  were inversely related and the *REDUB* for the  
597 mixed pixel was the minimum depth in the database because

the increased  $L_u$  associated with the limestone substrate  
caused the pixel to appear shallower than a streambed  
completely covered by periphyton. Only in the NIR were  
differences in  $f_p$  expressed in the *REDUB*, with higher  $f_p$   
corresponding to greater *REDUB* as the radiance contribu-  
tion from the limestone portion of the pixel was reduced,  
although the *REDUB* consistently underestimated the actual  
depth. This convergence in the NIR could be due to the  
more similar reflectance of the limestone and periphyton  
substrates at these wavelengths and/or due to stronger  
absorption by the water itself, which subdues the effect of  
bottom albedo on  $L_u$ .

An opposite pattern was observed when the pure lime-  
stone substrate end member was used as the reference for  
*REDUB* retrievals from the simulated periphyton/limestone  
mixtures. In this case, *REDUB* spectra were more sensitive

598  
599  
600  
601  
602  
603  
604  
605  
606  
607  
608  
609  
610  
611  
612  
613

614 to  $f_p$  but still tended to saturate and take on the value of the  
 615 deepest depth within the database for wavelengths extend-  
 616 ing throughout the red portion of the spectrum for high  $f_p$ .  
 617 The lower bottom albedo of the periphyton substrate  
 618 reduced  $L_u$  for the mixed pixel and therefore caused the  
 619 bottom to appear deeper than would a periphyton-free  
 620 limestone substrate, and at an actual depth of 30 cm,  
 621 REDUB overestimated  $z_b$  by up to 50 cm in the green region  
 622 of the spectrum even when  $f_p$  was only 0.2. The crossover at  
 623 560 nm was absent when pure limestone was used as a  
 624 reference because, unlike the darker periphyton, the  
 625 reflectance of the limestone substrate exceeded the scatter-  
 626 ing-induced volume reflectance of the water column,  
 627 illustrating the importance of bottom contrast for depth  
 628 retrieval. The REDUB also overestimated the true depth  
 629 throughout the red and NIR and only at wavelengths of 720  
 630 nm or greater, where transmittance through the water  
 631 column was reduced and the reflectance difference between  
 632 limestone and periphyton less pronounced, did the REDUB  
 633 begin to converge on the true depth. These results indicate  
 634 that two different estimates of depth would be retrieved,  
 635 depending on which pure substrate served as a reference:  
 636 depth would be overestimated at all wavelengths if lime-  
 637 stone were assumed and would be either over-(short  
 638 wavelengths) or underestimated (long wavelengths) if a  
 639 periphyton-coated streambed was assumed instead.

640 In contrast to the sensitivity of the wavelength-specific  
 641 REDUB spectra to mixed substrates, the REDUB ratio was  
 642 much more robust to sub-pixel substrate heterogeneity  
 643 (points in Fig. 7b–e, referring to the top  $x$ -axis of each  
 644 panel). For an actual depth of 30 cm, the REDUB ratio  
 645 consistently reproduced the actual  $z_b$  regardless of whether  
 646 the periphyton or limestone database was used as a  
 647 reference. For mixed substrates at a depth of 60 cm, the  
 648 REDUB ratio retrieved from the periphyton database over-  
 649 estimated  $z_b$  by up to 10 cm for small  $f_p$  but agreement  
 650 improved for larger  $f_p$ . When the limestone database served  
 651 as the reference, the REDUB ratio reproduced  $z_b$  for small  $f_p$   
 652 and underestimated  $z_b$  by only 3 cm for large  $f_p$ .

### 653 3.4. Stream bank spectral mixture analysis

654 Fig. 8a and b illustrate the simple geometric representa-  
 655 tions of gravel bars and vegetated cutbanks used to simulate  
 656 mixed streamside pixels as weighted linear combinations of  
 657 the pure spectra for each bank material and the submerged  
 658 channel bed. For the vegetated cutbank simulations, we used  
 659 the Hydrolight spectrum corresponding to depth of the  
 660 adjacent streambed as the aquatic end member. For the  
 661 gravel bar mixture models, we considered spectra for three  
 662 depths: 1) the mean depth along the bed slope off of the bar,  
 663 which thus varied depending on  $\theta_b$  and  $f_b$ ; 2) a fixed,  
 664 moderate depth ( $z_b=0.2$  or  $0.4$  m); and 3) 1.5 m, the greatest  
 665 depth in the Hydrolight database (a hypothetical infinitely  
 666 deep-water column produced nearly identical results). The  
 667 actual (simulated) and modeled bank fractions  $f_b$  for four

morphologic scenarios, computed using linear, unit sum-  
 constrained two-end member models are plotted in panels  
 c–f. Fig. 8c and e indicate that for gravel bars the modeled  
 bank fraction is accurate to within a few percent for large  $f_b$   
 but is consistently underestimated for water-dominated  
 pixels. The magnitude of this error increases as  $f_b$  decreases,  
 with negative modeled bank fractions for the smallest actual  
 $f_b$ . Fraction errors were smaller, however, when a moderate  
 fixed depth end member was used rather than the mean  
 depth along the slope; using a deep-water spectrum further  
 reduced the fraction error. These results imply that shallow-  
 water spectra along gradually sloping bars tend to be very  
 similar to exposed, possibly moist, gravel, and that more  
 accurate unmixing of stream bank pixels could be achieved  
 by selecting or modeling a deep-water end member with  
 greater spectral contrast.

Although the radiance contribution from the exposed  
 portion of a mixed pixel might be expected to overwhelm  
 the submerged area and lead to overestimated, possibly  
 super-positive bank fractions,  $f_b$  was underestimated for our  
 simulated mixtures and became negative at low  $f_b$ , even  
 when a deep-water end member was used. We attribute this  
 counterintuitive result to the use of relatively bright, dry  
 gravel as a terrestrial end member but dark, wet gravel to  
 define the bottom albedo for the water spectra (Fig. 1). This  
 low reflectance substrate was actually darker than deep,  
 open water due to volume scattering within the water  
 column. Mixed pixels comprised primarily of water were  
 therefore brighter than shallow water end members bearing  
 the imprint of the dark gravel substrate, which dictated that  
 the bright terrestrial end member would require a negative  
 fraction in order to make the modeled mixture dark enough  
 while still honoring the unit sum constraint. This effect was  
 most pronounced for the smallest actual  $f_b$  and steepest bar  
 slopes, which contained the most (and deepest) water and  
 were thus brightest at the pixel scale. The extreme case is  
 illustrated in Fig. 8g, where a pixel containing only 10%  
 gravel bar was unmixed using a shallow water end member  
 that was actually brighter than the pixel-scale mixture,  
 resulting in a large negative modeled  $f_b$  and a 25% fraction  
 error. Had a brighter substrate (i.e., limestone) been used to  
 define the bottom albedo, the shallow water end members  
 would have been brighter than open water, resulting in  
 overestimated bank fractions. The choice of a terrestrial end  
 member could also play a role, with bright spectra from  
 high, dry bar tops producing different results, typically  
 underestimated bank fractions, than darker spectra from  
 lower on the bar surface, where wet sand might also be  
 present. These results indicate that linear spectral unmixing  
 of gravel bars is highly sensitive to end member selection  
 and thus subject to considerable uncertainty.

For vegetated cutbanks, typically found opposite gravel  
 point bars along the outside of meander bends, linear  
 spectral unmixing of stream bank pixels appears much more  
 promising. For actual bank fractions ranging from 0.1 to 0.9  
 and bed depths of 20 and 40 cm, the modeled  $f_b$  reproduce



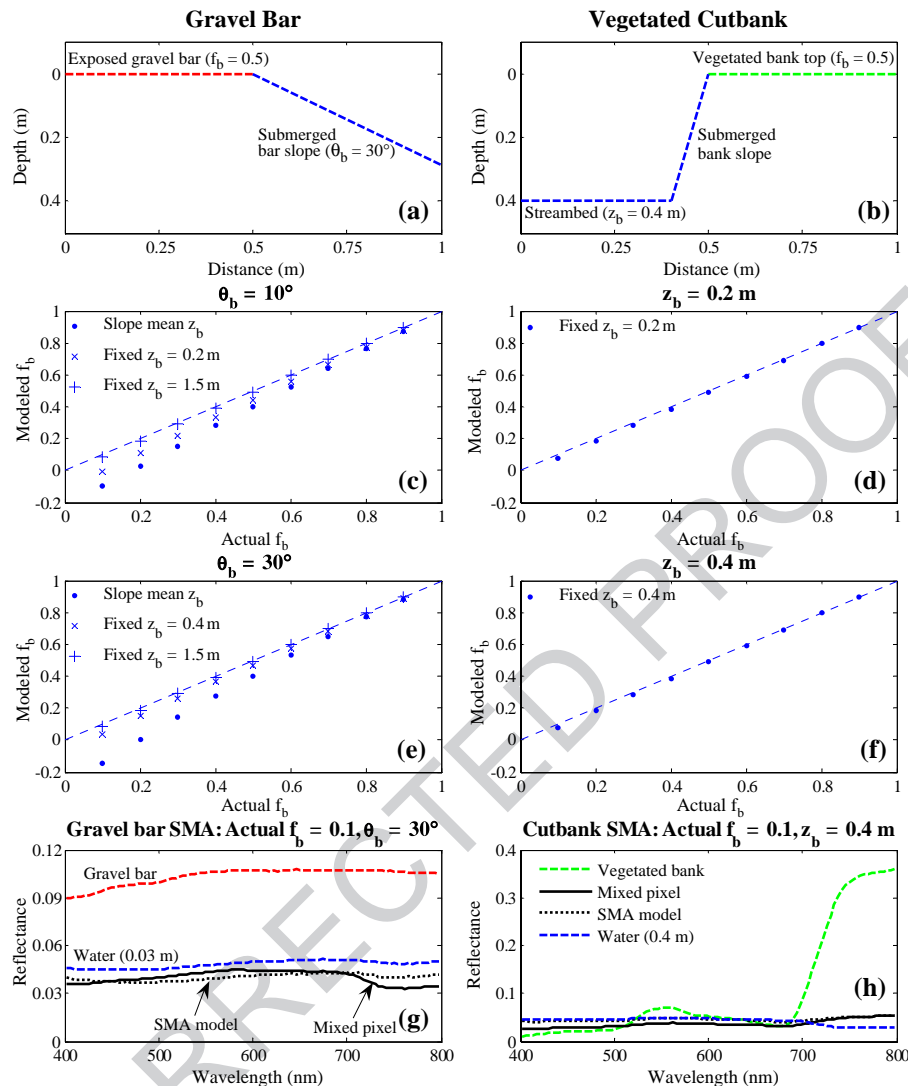


Fig. 8. Spectral characteristics of mixed terrestrial/aquatic pixels along stream banks. Geometric configuration of simulated gravel bars (a) and vegetated cutbanks (b), with plots of the actual and modeled bank fractions  $f_b$  for each morphologic scenario and end member pair shown in panels (c)–(f); dashed lines represent the 1:1 line where the modeled  $f_b$  reproduces the actual  $f_b$  for the simulation. Panels (g) and (h) illustrate the end member spectra, simulated mixed pixels, and SMA-modeled mixtures for the case of small  $f_b$ .

724 the fractions used to simulate the mixtures almost exactly,  
 725 even for the small actual bank fractions that proved most  
 726 problematic for gravel bars (Fig. 8h). Unlike gravel bars  
 727 with reflectance spectra similar to the adjacent substrate,  
 728 vegetation along the banks is quite spectrally distinct from  
 729 aquatic end members, particularly in the near-infrared. This  
 730 enhanced spectral contrast allows for accurate solution of  
 731 the mixing model and also reduces the sensitivity of the  
 732 resulting fractions to end member selection.

### 733 3.5. Application to the Lamar River AISA scene

734 The simulations described in the preceding sections were  
 735 motivated by our field experience in the Lamar River Basin  
 736 and by the need to establish a physically-based theoretical  
 737 foundation for analyzing archival image data for which field  
 738 measurements were unavailable. As an example of the

importance and applicability of our simulation-based results,  
 we developed a ratio-based relative depth map and two-end  
 member spectral mixture models from an AISA hyper-  
 spectral image of the Lamar River (Fig. 9a). A relative depth  
 value was assigned to each in-stream pixel by 1) computing  
 the natural logarithm of the ratio of apparent reflectances  
 (Section 2.1) measured in spectral bands centered at 555 and  
 693 nm to obtain a variable linearly related to water depth;  
 2) subtracting the minimum ratio value from every pixel, in  
 effect setting the minimum depth to zero; and 3) dividing  
 each pixel by the mean of all in-stream pixels. The resulting  
 image (Fig. 9b) highlighted a shallow gravel bar on the left  
 side of the channel and a narrow talweg along the outer  
 bank, illustrating the complex, fine-scale morphology  
 typical of this dynamic fluvial system. The relatively coarse  
 image data dictated that this filtered, 2.5 m representation of  
 the true bed topography would include a large proportion of

739  
 740  
 741  
 742  
 743  
 744  
 745  
 746  
 747  
 748  
 749  
 750  
 751  
 752  
 753  
 754  
 755

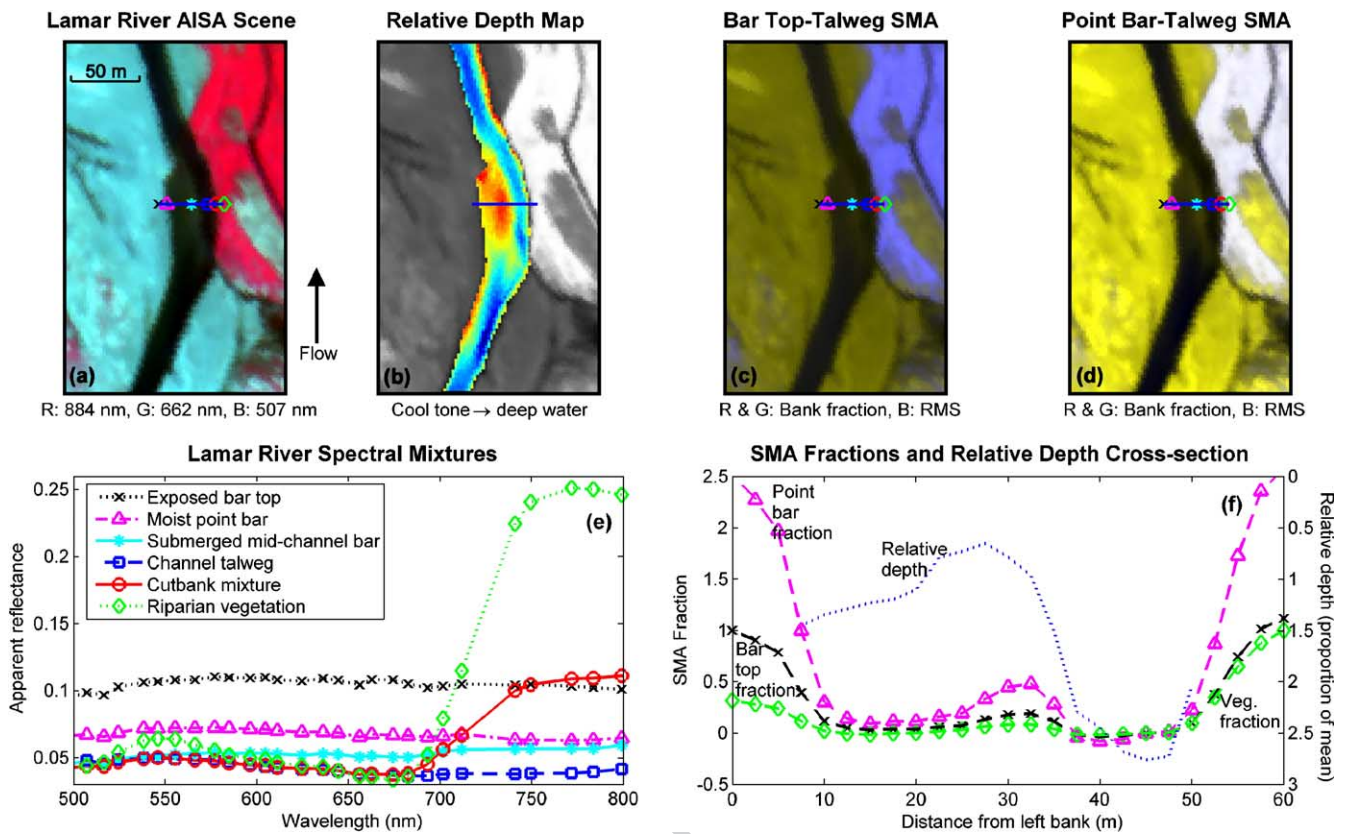


Fig. 9. (a) AISA hyperspectral image of the Lamar River; (b) relative depth map with cooler tones indicating deeper water (background is the 884 nm band); (c) stream bank mixture models for the exposed bar top and (d) moist point bar end members; (e) apparent reflectance spectra extracted along the transect shown with the blue line in (a–d); and (f) modeled fractions (left axis) and relative depth cross-section (right axis).

756 variable depth pixels analogous to our simulations. These  
 757 morphologic scenarios provided theoretical evidence that  
 758 the log-transformed band ratio provides an unbiased  
 759 estimate of the pixel-scale mean depth, although replacing  
 760 point measurements of depth with an area-weighted average  
 761 will inevitably entail a loss of information (i.e., reduction in  
 762 variance). The simulations thus justified our interpretation  
 763 of image-derived depth maps while also informing us of  
 764 their limitations and inherent uncertainties.

765 Similarly, two-end member spectral mixture models of  
 766 the Lamar River were consistent with the results obtained  
 767 for simulated stream bank mixtures (Section 3.4). We  
 768 created models that unmix the wetted channel from 1)  
 769 the exposed, presumably dry bar top; 2) the point bar  
 770 immediately adjacent to the channel, which was probably  
 771 somewhat moist; and 3) riparian vegetation on top of the  
 772 outside cutbank. A single water end member was selected  
 773 from the talweg and a unit-sum constraint was included in  
 774 all three models. As predicted by our simulations, the high  
 775 spectral contrast between the channel and the vegetated  
 776 cutbank ensured accurate unmixing on the right side of  
 777 the river, as indicated by near-unity vegetation fractions (Fig.  
 778 9f) and low RMS errors (not shown). The two bar–channel  
 779 mixture models are displayed as false-color composites in  
 780 Fig. 9c and d, and, as expected, the gradually sloping left  
 781 margin of the river proved more problematic. Although the

782 two bar end members resulted in fraction images with  
 783 similar spatial patterns, the bank fraction estimated using the  
 784 dark point bar was consistently higher than when a brighter,  
 785 bar top spectrum served as the terrestrial end member; this is  
 786 expressed as a darker and/or greener tone in Fig. 9c relative  
 787 to d, which has an identical contrast stretch. The darkness of  
 788 the wetted channel in these images indicates very small,  
 789 mostly negative, bank fractions and small RMS errors,  
 790 suggesting that relatively deep water can be distinguished  
 791 from either bar end member. For the shallow mid-channel  
 792 bar, however, the slightly lighter, yellow tone indicates a  
 793 larger bank fraction and suggests that water depth has a  
 794 confounding effect on linear mixture models. On the  
 795 opposite, densely vegetated bank, the blue hue in Fig. 9c  
 796 represents large RMS errors when the brighter, bar top end  
 797 member was used, while the white area of 9d indicates both  
 798 large RMS errors and super-positive bank fractions for the  
 799 darker, point bar end member. Both of these images suggest  
 800 that simple two-end member models failed to provide a  
 801 complete description of the riparian environment.

802 The image spectra in Fig. 9e confirmed that accurate  
 803 unmixing of stream banks was favored by the large NIR  
 804 reflectance difference between the channel and adjacent  
 805 riparian vegetation and compromised by the similar spectral  
 806 shapes for submerged and exposed portions of gravel bars,  
 807 which appeared to differ only in overall brightness. The

808 difficulty of unmixing bar–channel mixtures could be due to  
809 both a lack of spectral contrast and the “visibility” of the  
810 terrestrial end member through shallow water, resulting in  
811 considerable spectral confusion. This hypothesis was  
812 supported by the cross-sections of relative depth and end  
813 member fractions in Fig. 9f, where the bar fractions for both  
814 end members mimic the channel geometry, notably the mid-  
815 channel bar, revealed by the log-transformed band ratio,  
816 with a gradual transition to high bar fractions along the left  
817 bank.

## 818 4. Discussion

### 819 4.1. Limitations and applicability

820 The first-order analysis presented in this study provided  
821 an indication of the likely effects of sub-pixel variability of  
822 depth and/or bottom albedo and stream bank spectral  
823 mixtures upon image-derived depth estimates, but our  
824 approach was limited in several important respects. First,  
825 our representation of the water column optical properties  
826 was simplistic and could be refined by incorporating  
827 chlorophyll, dissolved organic matter, and vertical concen-  
828 tration gradients; in situ measurements of absorption and  
829 scattering coefficients would be invaluable. Second, our  
830 simulated pixels did not incorporate sensor spectral response  
831 or point spread function and assumed linear mixing,  
832 ignoring in-water adjacency effects. We also did not  
833 consider the case where both depth and substrate vary  
834 simultaneously on a sub-pixel scale. Sensor characteristics  
835 could be included with appropriate technical data, but the  
836 problems of intimate mixtures and co-varying depth and  
837 bottom albedo present greater challenges. Finally, our  
838 simulations were based on only a handful of measured  
839 spectra from one small stream in Yellowstone National Park  
840 and these bank material and substrate end members might  
841 not be representative of other rivers in different environ-  
842 ments. Nevertheless, we believe that the analysis presented  
843 here is sufficiently general to illustrate, in a physically-based  
844 manner, important relationships among channel morphol-  
845 ogy, sensor spatial resolution, and the uncertainty inherent  
846 to spectrally-based depth retrieval.

### 847 4.2. Advantages of ratio-based depth retrieval

848 The results outlined above demonstrated the utility of the  
849 log-transformed band ratio for estimating water depth and  
850 indicated that the technique is particularly well-suited to  
851 complex fluvial environments like the Lamar River. A  
852 primary advantage of the ratio-based algorithm is that the  
853 site-specific normalization inherent to the ratio implicitly  
854 accounts for solar geometry and specular reflection from the  
855 water surface. Because this surface reflectance is spectrally  
856 flat (Legleiter et al., 2004), it will affect both bands equally  
857 and cancel during the ratio calculation. Unlike oceano-

858 graphic applications where sun glint can be attributed 858  
859 primarily to wind-induced waves and corrected uniformly 859  
860 across an image, pixel-by-pixel removal of the specular 860  
861 component of the upwelling radiance is critical in rivers 861  
862 because the flow-related turbulence responsible for the 862  
863 irregularity of the water surface varies spatially as a function 863  
864 of depth, velocity, and substrate particle size. 864

865 Similarly, although the topographic effects described in 865  
866 Section 3.1 could severely compromise analyses based on 866  
867 the absolute magnitude of  $L_u$ , ratio-based depth retrieval 867  
868 algorithms should be less affected. Because the incidence 868  
869 angle terms in Eq. (2) are spectrally invariant and occur in 869  
870 both the numerator and denominator, bed topography will 870  
871 be implicitly accounted for in each individual pixel. The 871  
872 accuracy and precision of image-derived estimates will still 872  
873 be lower in areas with steep bed slopes and/or an 873  
874 unfavorable aspect because  $E_d$  and thus  $L_u$  will be reduced. 874  
875 When the bed is poorly illuminated, changes in depth will 875  
876 correspond to very small changes in  $L_u$  that could be below 876  
877 the detection limit of many imaging systems (Legleiter et 877  
878 al., 2004). Because streambed slope and aspect are spatially 878  
879 variable, the magnitude of these topographic effects will 879  
880 also vary throughout an image to an extent that will not, in 880  
881 practice, be known a priori. Acquiring data at lower  $\theta_s$  will 881  
882 reduce topographic effects but could introduce problems 882  
883 (i.e., sensor saturation) related to specular reflection from 883  
884 the water surface; Mobley (1999) cautions that sun glint is 884  
885 inevitable when both solar and view zenith angles are 885  
886 small. Collecting data at off-nadir views could mitigate this 886  
887 effect but might complicate flight planning and geometric 887  
888 correction. 888

889 Our simulations of beta-distributed depths and substrate 889  
890 patches also suggested that ratio-based depth retrieval is 890  
891 robust to fine-scale bottom morphology and substrate 891  
892 heterogeneity. Whereas the *REDUB* spectra calculated for 892  
893 stepped streambeds were subject to a strong, spectrally- 893  
894 dependent bias toward shallower water, the *REDUB* ratio 894  
895 consistently reproduced the area-weighted mean depth for 895  
896 uniform, symmetric, and highly skewed depth distributions. 896  
897 When bright limestone and dark periphyton substrates were 897  
898 combined in varying proportions at a fixed depth, the 898  
899 spectral *REDUB* was again strongly biased while the 899  
900 *REDUB* ratio reproduced the actual depth for shallow water 900  
901 and produced relatively small errors in deep water. The 901  
902 robustness of the band ratio in these simulations reflects the 902  
903 theoretical basis of the technique—whereas a change in 903  
904 substrate reflectance affects both ratio bands similarly, an 904  
905 increase in depth produces a much greater decrease in 905  
906 radiance in the band with stronger attenuation (Dierssen et 906  
907 al., 2003). Our results support the finding of Stumpf et al. 907  
908 (2003) that ratio values for different substrates at similar 908  
909 depths are similar to one another and imply that the ratio- 909  
910 based algorithm is more appropriate for complex in-stream 910  
911 habitats than alternative approaches that do not include such 911  
912 normalization. For example, the comparative spectral 912  
913 classification method of Louchard et al. (2003), which 913



914 assigns depth and substrate reflectance values to image  
 915 pixels by selecting the Hydrolight-modeled spectrum most  
 916 similar to the radiance measured by the imaging system,  
 917 might not be able to account for spatial variations in  
 918 specular reflectance and bottom slope and could also be  
 919 sensitive to sub-pixel mixtures of depth and/or bottom  
 920 albedo. Although this type of sophisticated spectrally-based  
 921 analysis could prove useful in the future, at present the ratio-  
 922 based algorithm provides a simple, effective method for  
 923 mapping river channel morphology.

#### 924 4.3. Problems and prospects for spectral mixture analysis

925 The simple, two-end member models for mixed pixels  
 926 along stream banks described in Section 3.4 and applied to a  
 927 hyperspectral image of the Lamar River in Section 3.5  
 928 indicated that the ability to unmix streamside spectra is  
 929 strongly dependent on bank morphology. Specifically,  
 930 whereas bank fractions for vegetated cutbanks were  
 931 modeled very accurately, spectral mixture models developed  
 932 for gravel bars typically featured relatively large fraction  
 933 errors. The differences between these two bank types  
 934 illustrated the importance of spectral contrast and demon-  
 935 strated the difficulty of discriminating between a shallow,  
 936 submerged gravel bed and an adjacent, exposed bar surface.  
 937 Our analysis of the gravel bar scenario also indicated that  $f_b$   
 938 estimates were sensitive to the selection of both terrestrial  
 939 and aquatic end members, with smaller fraction errors for  
 940 deep-water spectra and bank fraction overestimates asso-  
 941 ciated with darker terrestrial spectra. These results clearly  
 942 indicate that a greater degree of confidence can be assigned  
 943 to mixture models developed for steep, vegetated banks than  
 944 for gradually sloping gravel bars. This finding implies that  
 945 spectral mixture analysis will be a more reliable tool for  
 946 some channel morphologies, such as meandering meadow  
 947 streams with cohesive banks, than for others, such as  
 948 bedload-dominated braided channels with numerous gravel  
 949 bars.

950 The sensitivity to both morphology and end member  
 951 selection observed in our simulations implies that more  
 952 sophisticated multiple end member spectral mixture analysis  
 953 (MESMA), in which the end members used to model mixed  
 954 spectra are allowed to vary on a pixel-by-pixel basis  
 955 (Roberts et al., 1998), might be a more appropriate method  
 956 for fluvial environments. By coupling bank and substrate  
 957 spectra with a radiative transfer model such as Hydrolight,  
 958 MESMA could also be useful for depth retrieval. Hedley  
 959 and Mumby (2003) have proposed an SMA-based method  
 960 of mapping depth and sub-pixel proportions of benthic end  
 961 members, but their approach does not provide any measure  
 962 of the error in the mixture model (e.g., root mean square  
 963 error or spectral residuals; see Roberts et al., 1998) and has  
 964 not yet been tested on real data. Future application of SMA  
 965 to rivers will require the development of more extensive  
 966 substrate spectral libraries and the acquisition of more  
 967 advanced, hyperspectral image data, which should involve

careful evaluation of the tradeoffs among spectral detail, 968  
 spatial resolution, and radiometric precision. 969

#### 4.4. Implications for remote measurement of river channel 970 change 971

The fundamental motivation for this study was to 972  
 determine whether remotely sensed data could be used to 973  
 estimate water depth with sufficient accuracy and precision 974  
 to document subtle changes in channel morphology. Our 975  
 results indicate that this important question cannot be 976  
 answered with broad generalizations but must instead be 977  
 addressed on a case-by-case basis. The analysis of simple 978  
 morphologic scenarios presented here illustrated how 979  
 streambed slope and aspect, bed topography, and substrate 980  
 heterogeneity influence the upwelling spectral radiance 981  
 from a shallow stream channel. These simulations also 982  
 suggested, however, that the simple, ratio-based depth 983  
 retrieval algorithm is robust and well-suited for complex 984  
 fluvial systems, consistently reproducing the area-weighted 985  
 mean depth when depth and/or substrate vary on a sub-pixel 986  
 scale. The ratio calculation also implicitly accounts for 987  
 specular reflectance and topographic effects, but solar- 988  
 streambed geometry could still adversely affect depth 989  
 retrieval at high solar zenith angles and/or where the bed 990  
 slopes away from the sun. In topographically complex 991  
 meandering rivers, the resolution and reliability of depth 992  
 estimates could thus vary from one pixel to the next. 993

In fact, the primary implication of our study is that the 994  
 relationship between sensor spatial resolution and channel 995  
 morphology establishes a set of complex, spatially variable 996  
 controls on the accuracy and precision with which river 997  
 channels can be remotely mapped. For example, both our 998  
 simulations and the mixture models we derived from the 999  
 Lamar River hyperspectral image indicate a strong morpho- 1000  
 logic dependence, with SMA-derived bank fractions esti- 1001  
 mated more accurately for steep, vegetated banks than for 1002  
 gravel bars. This effect is, of course, mediated by sensor 1003  
 spatial resolution because the proportion of mixed terres- 1004  
 trial/aquatic pixels will decrease as the ratio of channel 1005  
 width to image pixel size increases. For the fluvial 1006  
 geomorphologist, these results imply that sub-pixel refine- 1007  
 ment of width measurements (i.e., multiplying  $f_b$  by the 1008  
 pixel size for the end-points of a cross-section) will likely be 1009  
 more accurate along the outer bank of a meander bend than 1010  
 along the opposite point bar. If this hypothesized pattern 1011  
 holds true, a greater degree of confidence can be assigned to 1012  
 lateral migration and pool scour along the outer bank than to 1013  
 point bar growth and bed aggradation on the inner bank. 1014  
 Within the channel proper, the ability to obtain realistic 1015  
 representations of pools, riffles, and other habitat features 1016  
 from digital image data will depend in a complex and 1017  
 spatially variable manner upon both the spatial resolution of 1018  
 the imaging system and the typical dimensions of channel 1019  
 features. If the spatial frequency of bed elevation change 1020  
 within the channel exceeds the sampling frequency of the 1021



1022 sensor, morphologic detail will be obscured, with the  
1023 discrepancy between representation and reality becoming  
1024 more pronounced as this frequency difference increases. In  
1025 essence, the morphology of the channel complicates  
1026 attempts to document that morphology using remote sensing  
1027 techniques, and a spatial resolution that is adequate for one  
1028 reach might not be appropriate for other, more complex  
1029 channel segments.

1030 Given this intimate linkage between sensor spatial  
1031 resolution and channel morphology, the selection of an  
1032 appropriate pixel size for specific studies becomes an  
1033 important practical question. Because the log-transformed  
1034 band ratio could provide an unbiased estimate of the area-  
1035 weighted pixel-scale mean depth, the choice of a spatial  
1036 resolution does not necessarily need to involve radiative  
1037 transfer models or complicated hydrologic optics but can  
1038 instead be posed in terms of sample design. Efficient use of  
1039 remotely sensed data for river research and management  
1040 will require familiarity with the channels of interest along  
1041 with clear statements of the specific objectives of each  
1042 study. We propose that although the accuracy and precision  
1043 of image-derived depth estimates are complicated, spatially  
1044 variable functions of channel morphology and sensor  
1045 characteristics, they are nonetheless governed by funda-  
1046 mental physical processes which can be modeled to quantify  
1047 the resolution and reliability of spectrally-based depth  
1048 retrieval. Research toward this goal is needed to develop  
1049 operational guidelines and define realistic expectations for  
1050 remote sensing of rivers.

## 1051 5. Conclusion

1052 The contribution of remote sensing technology to river  
1053 research depends on the ability to obtain from digital  
1054 image data quantitative information on the channel  
1055 characteristics of interest with the accuracy and precision  
1056 required by specific applications. In this study, we  
1057 evaluated the effects of sub-pixel variations in depth and  
1058 bottom albedo on image-derived depth estimates and the  
1059 role of morphology and end member selection in spectral  
1060 mixture analysis of stream bank pixels. Using a radiative  
1061 transfer model, we generated a database of spectra for  
1062 various depths and substrate types, which we then coupled  
1063 (assuming linear mixing) to various morphologic scenarios  
1064 including a planar sloping streambed, a stepped bed, beta  
1065 distributions of fine-scale depths, and heterogeneous  
1066 substrates. These simulations indicated that although the  
1067 upwelling spectral radiance from a shallow stream channel  
1068 can be highly sensitive to each of these factors, simple,  
1069 ratio-based depth retrieval algorithms are robust to topo-  
1070 graphic effects, fine-scale bottom morphology, and patchy  
1071 substrates. For mixed pixels along channel margins, our  
1072 results indicated that bank fractions derived from two-end  
1073 member mixture models were highly accurate for vegetated  
1074 cutbanks but less reliable for gravel bars. These theoretical

1075 results were tested by producing a relative depth map and  
1076 calculating bank and water fractions from a hyperspectral  
1077 image of the Lamar River. The primary conclusions of this  
1078 study are that the utility of remotely sensed data for  
1079 characterizing fluvial environments depends strongly on  
1080 the relationship between sensor spatial resolution and  
1081 channel morphology and that the accuracy and precision  
1082 of image-derived depth estimates are spatially variable and  
1083 cannot be categorically defined. The ability of the ratio-  
1084 based depth retrieval to consistently reproduce the area-  
1085 weighted, pixel-scale mean depth for our simulated  
1086 morphologic scenarios was encouraging, however, and  
1087 future research will focus on developing methods for  
1088 selecting an appropriate pixel size for different types of  
1089 channels. A related goal crucial for application-oriented  
1090 users of digital image data is to provide physically-based,  
1091 quantitative estimates of the uncertainty inherent to remote  
1092 mapping of river channel morphology.

## Acknowledgement

1093 Andrew Marcus provided the spectroradiometer and  
1094 thought-provoking discussions out on the stream in Yellow-  
1095 stone National Park. Additional help in the field was  
1096 provided by Mark Fonstad, Kyle Legleiter, Annie Toth,  
1097 Sharolyn Anderson, Will Jensen, Lorin Groshong, and Lisa,  
1098 Alexandra, Rebecca and Geoffrey Marcus. The Hydrolight  
1099 model was developed by Curt Mobley of Sequoia Scientific,  
1100 and Lydia Sundman provided valuable implementation  
1101 advice. Rick Lawrence and Mike Zambon of Montana State  
1102 University made the Lamar River AISA image available to  
1103 us; these data were acquired through a grant from the  
1104 Environmental Protection Agency. Bob Crabtree of the  
1105 Yellowstone Ecological Center provided logistical support.  
1106 Funding sources included fellowships from the American  
1107 Society for Engineering Education, the National Science  
1108 Foundation, and the American Society for Photogrammetry  
1109 and Remote Sensing and grants from the Water Resources  
1110 Specialty Group of the Association of American Geogra-  
1111 phers, the California Space Institute, and the Graduate  
1112 Division at UC Santa Barbara. The thoughtful comments of  
1113 two anonymous reviewers also resulted in an improved final  
1114 paper.  
1115

## References

- 1116  
1117  
1118  
1119  
1120  
1121  
1122  
1123  
1124  
1125  
1126
- Adams, J. B., Smith, M. O., & Gillespie, A. R. (1993). Imaging spectroscopy: Interpretation based on spectral mixture analysis. In C. M. Pieters, & P. A. J. Englert (Eds.), *Remote geochemical analysis: Elemental and mineralogical composition* (pp. 145–166). Cambridge: Press Syndicate of University of Cambridge.
- Andrefouet, S., Berkelmans, R., Odriozola, L., Done, T., Oliver, J., & Muller-Karger, F. (2002). Choosing the appropriate spatial resolution for monitoring coral bleaching events using remote sensing. *Coral Reefs*, 21, 147–154.

- 1127 Andrefouet, S., Kramer, P., Torres-Pulliza, D., Joyce, K. E., Hochberg, E. J.,  
1128 Garza-Perez, R., et al. (2003). Multi-site evaluation of IKONOS data for  
1129 classification of tropical coral reef environments. *Remote Sensing of*  
1130 *Environment*, 88, 128–143.
- 1131 Ashmore, P. E., & Church, M. (1998). Sediment transport and river  
1132 morphology: A paradigm for study. In J. B. Bradley (Ed.), *Gravel-bed*  
1133 *ivers in the environment* (pp. 115–140). Highlands Ranch, CO: Water  
1134 Resources Publications.
- 1135 Bryant, R. G., & Gilvear, D. J. (1999). Quantifying geomorphic and  
1136 riparian land cover changes either side of a large flood event using  
1137 airborne remote sensing: River Tay, Scotland. *Geomorphology*, 29,  
1138 307–321.
- 1139 Bukata, R. P., Jerome, J. H., Kondratyev, K. Y., & Pozdnyakov, D. V.  
1140 (1995). *Optical Properties and Remote Sensing of Inland and Coastal*  
1141 *Waters* (p. 362). Boca Raton, FL: CRC Press.
- 1142 Cox, C., & Munk, W. (1954). The measurement of the roughness of the of  
1143 the sea surface from photographs of the sun's glitter. *Journal of the*  
1144 *Optical Society of America*, 44, 838–850.
- 1145 Cracknell, A. P. (1998). Synergy in remote sensing—What's in a pixel?  
1146 *International Journal of Remote Sensing*, 19, 2025–2047.
- 1147 Devore, J. L. (2000). *Probability and Statistics for Engineering and the*  
1148 *Sciences* (p. 775). Pacific Grove, CA: Duxbury.
- 1149 Dierssen, H. M., Zimmerman, R. C., Leathers, R. A., Downes, T. V., &  
1150 Davis, C. O. (2003). Ocean color remote sensing of seagrass and  
1151 bathymetry in the Bahamas Banks by high-resolution airborne imagery.  
1152 *Limnology and Oceanography*, 48, 444–455.
- 1153 Downs, P. W., & Kondolf, G. M. (2002). Post-project appraisals in adaptive  
1154 management of river channel restoration. *Environmental Management*,  
1155 29, 477–496.
- 1156 Gaeuman, D. A., Schmidt, J. C., & Wilcock, P. R. (2003). Evaluation of in-  
1157 channel gravel storage with morphology-based gravel budgets devel-  
1158 oped from planimetric data. *Journal of Geophysical Research—Earth*  
1159 *Surface*, 108, 6001.
- 1160 Gregg, W. W., & Carder, K. (1990). A simple spectral solar irradiance  
1161 model for cloudless maritime atmospheres. *Limnology and Ocean-*  
1162 *ography*, 35, 1657–1675.
- 1163 Harrison, A. W., & Coombes, C. A. (1988). An opaque cloud cover model  
1164 of sky short wavelength radiance. *Solar Energy*, 41, 387–392.
- 1165 Hedley, J. D., & Mumby, P. J. (2003). A remote sensing method for  
1166 resolving depth and subpixel composition of aquatic benthos. *Limnol-*  
1167 *ogy and Oceanography*, 48, 480–488.
- 1168 Hedley, J. D., Mumby, P. J., Joyce, K. E., & Phinn, S. R. (2004). Spectral  
1169 unmixing of coral reef benthos under ideal conditions. *Coral Reefs*, 23,  
1170 60–73.
- 1171 Lane, S. N. (1998). The use of digital terrain modelling in the under-  
1172 standing of dynamic river channel systems. In J. H. Chandler (Ed.),  
1173 *Landform monitoring, modelling and analysis* (pp. 311–342). New  
1174 York: John Wiley and Sons.
- 1175 Lane, S. N., Westaway, R. M., & Hicks, D. M. (2003). Estimation of  
1176 erosion and deposition volumes in a large, gravel-bed, braided river  
1177 using synoptic remote sensing. *Earth Surface Processes and Land-*  
1178 *forms*, 28, 249–271.
- 1179 Legleiter, C. J., & Goodchild, M. F. (in press). Alternative representations  
1180 of in-stream habitat: Classification using remotely sensed data,  
1181 hydraulic modeling, and fuzzy logic. *International Journal of Geo-*  
1182 *graphical Information Science*.
- 1183 Legleiter, C. J., Marcus, W. A., & Lawrence, R. (2002). Effects of sensor  
1184 resolution on mapping in-stream habitats. *Photogrammetric Engineer-*  
1185 *ing and Remote Sensing*, 68, 801–807.
- Legleiter, C. J., Roberts, D. A., Marcus, W. A., & Fonstad, M. A. (2004). 1186  
Passive optical remote sensing of river channel morphology and in- 1187  
stream habitat: Physical basis and feasibility. *Remote Sensing of* 1188  
*Environment*, 93, 493–510. 1189
- Louchard, E. M., Leathers, R. A., Downes, T. V., Reid, R. P., Stephens, F. 1190  
C., & Davis, C. O. (2003). Optical remote sensing of benthic habitats 1191  
and bathymetry in coastal environments at Lee Stocking Island, 1192  
Bahamas: A comparative spectral classification approach. *Limnology* 1193  
*and Oceanography*, 48, 511–521. 1194
- Lyon, J. G., Lunetta, R. S., & Williams, D. C. (1992). Airborne 1195  
multispectral scanner data for evaluating bottom sediment types and 1196  
water depths of the St. Mary's River, Michigan. *Photogrammetric* 1197  
*Engineering and Remote Sensing*, 58, 951–956. 1198
- Marcus, W. A., Legleiter, C. J., Aspinall, R. J., Boardman, J. W., & 1199  
Crabtree, R. L. (2003). High spatial resolution hyperspectral mapping of 1200  
in-stream habitats, depths, and woody debris in mountain streams. 1201  
*Geomorphology*, 55, 363–380. 1202
- Mertes, L. A. K. (2002). Remote sensing of riverine landscapes. *Freshwater* 1203  
*Biology*, 47, 799–816. 1204
- Mertes, L. A. K., Smith, M. O., & Adams, J. B. (1993). Estimating 1205  
suspended sediment concentrations in surface waters of the Amazon 1206  
River wetlands from Landsat images. *Remote Sensing of Environment*, 1207  
43, 281–301. 1208
- Mobley, C. D. (1994). *Light and Water: Radiative Transfer in Natural* 1209  
*Waters* (p. 592). San Diego: Academic Press. 1210
- Mobley, C. D. (1999). Estimation of the remote-sensing reflectance from 1211  
above-surface measurements. *Applied Optics*, 38, 7442–7455. 1212
- Mobley, C. D., & Sundman, L. K. (2001). *Hydrolight 4.2 User's Guide* 1213  
(p. 88). Redmond, WA: Sequoia Scientific. 1214
- Mobley, C. D., & Sundman, L. K. (2003). Effects of optically shallow 1215  
bottoms on upwelling radiances: Inhomogeneous and sloping bottoms. 1216  
*Limnology and Oceanography*, 48, 329–336. 1217
- Prostka, H. J., Ruppel, E. T., & Christiansen, R. J. (1975). *Geologic map of* 1218  
*the Abiathar Peak Quadrangle, Yellowstone National Park, Wyoming*. 1219  
U.S. Geological Survey Geological Quadrangle Map GQ-1244, scale 1220  
1:62:500. 1221
- Roberts, D. A., Gardner, M., Church, R., Ustin, S., Scheer, G., & Green, R. 1222  
O. (1998). Mapping chaparral in the Santa Monica Mountains using 1223  
multiple endmember spectral mixture models. *Remote Sensing of* 1224  
*Environment*, 65, 267–279. 1225
- Stumpf, R. P., Holderied, K., & Sinclair, M. (2003). Determination of water 1226  
depth with high-resolution satellite imagery over variable bottom types. 1227  
*Limnology and Oceanography*, 48, 547–556. 1228
- Thompson, D. M., & Hoffman, K. S. (2001). Equilibrium pool dimensions 1229  
and sediment-sorting patterns in coarse-grained, New England chan- 1230  
nels. *Geomorphology*, 38, 301–316. 1231
- Whited, D., Stanford, J. A., & Kimball, J. S. (2002). Application of 1232  
airborne multispectral digital imagery to quantify riverine habitats at 1233  
different base flows. *River Research and Applications*, 18, 583–594. 1234
- Winterbottom, S. J., & Gilvear, D. J. (1997). Quantification of channel bed 1235  
morphology in gravel-bed rivers using airborne multispectral imagery 1236  
and aerial photography. *Regulated Rivers: Research and Management*, 1237  
13, 489–499. 1238
- Wright, A., Marcus, W. A., & Aspinall, R. (2000). Evaluation of 1239  
multispectral, fine scale digital imagery as a tool for mapping stream 1240  
morphology. *Geomorphology*, 33, 107–120. 1241
- Zaneveld, J. R. V., & Boss, E. (2003). The influence of bottom morphology 1242  
on reflectance: Theory and two-dimensional geometry model. *Limnol-* 1243  
*ogy and Oceanography*, 48, 374–379. 1244